

Chemical Science

Accepted Manuscript

This article can be cited before page numbers have been issued, to do this please use: D. Wang, J. Tao, H. Zhang, P. Zhang and F. Chen, *Chem. Sci.*, 2026, DOI: 10.1039/D6SC00783J.



This is an Accepted Manuscript, which has been through the Royal Society of Chemistry peer review process and has been accepted for publication.

Accepted Manuscripts are published online shortly after acceptance, before technical editing, formatting and proof reading. Using this free service, authors can make their results available to the community, in citable form, before we publish the edited article. We will replace this Accepted Manuscript with the edited and formatted Advance Article as soon as it is available.

You can find more information about Accepted Manuscripts in the [Information for Authors](#).

Please note that technical editing may introduce minor changes to the text and/or graphics, which may alter content. The journal's standard [Terms & Conditions](#) and the [Ethical guidelines](#) still apply. In no event shall the Royal Society of Chemistry be held responsible for any errors or omissions in this Accepted Manuscript or any consequences arising from the use of any information it contains.

ARTICLE

Local Polarization Strategy for Efficient Sacrificial-free Hydrogen Peroxide Photoproduction

Donghui Wang,^a Jin-Gang-Lu Tao,^a Haiyang Zhang,^a Po Zhang^a and Feng Chen^{*a}Received 00th January 20xx,
Accepted 00th January 20xx

DOI: 10.1039/x0xx00000x

Photocatalytic production of hydrogen peroxide (H₂O₂) from water and oxygen under sunlight offers a safe and sustainable alternative to traditional processes. However, the sluggish water oxidation reaction (WOR) often imposes kinetic limitations on the accompanying oxygen reduction reaction (ORR) in pure water systems. This research developed a series of tailored covalent organic frameworks (COFs) with localized polarization features to boost the reaction rates of WOR. By incorporating varying numbers of *sp*²-hybridized nitrogen atoms into a single benzene ring, a locally polarized electronic environment was established. In particular, the dual *sp*²-hybridized nitrogen atoms in pyrimidine units induce strong local polarization, which facilitates charge separation and activates adjacent C=C bonds as more favorable site for WOR. Together with the highly efficient ORR activity enabled by the two nitrogen atoms, the pyrimidine-functionalized TpDa demonstrates outstanding performance in a sacrificial-agent-free system, achieving an H₂O₂ production rate of 6.94 mmol g⁻¹ h⁻¹ and an apparent quantum yield (AQY) of 25.2%. This work establishes local polarization engineering as an effective strategy for optimizing COFs photocatalysts and highlights its potential for solar-driven chemical transformations.

Introduction

Photocatalytic H₂O₂ synthesis driven by sunlight under ambient conditions offers a promising alternative to traditional anthraquinone-based processes.^{1, 2} However, most reported photocatalysts rely on sacrificial reagents (e.g., isopropanol) to enhance efficiency,^{3, 4} which not only increases cost but also complicates subsequent separation and purification of H₂O₂.^{5, 6} Thus, the development of efficient photocatalysts that operate in sacrificial-agent-free systems is of paramount importance. In recent years, metal-free organic polymers such as graphitic carbon nitride (*g*-C₃N₄) derivatives,^{7, 8} resorcinol-formaldehydes (RFs)^{9, 10} and COFs¹¹⁻¹³ have emerged as promising photocatalysts owing to their low cost, high efficiency, and structural tunability. Among them, COFs are particularly attractive due to their well-defined molecular structures that allow rational active site design, extended π -conjugation for improved light harvesting, and intrinsic porosity that facilitates mass transport.^{14, 15} Despite these advantages, the photocatalytic efficiency of COF-based systems for sacrificial-agent-free H₂O₂ production remains unsatisfactory. One limitation arises from the kinetically sluggish water WOR, which provides the protons required for H₂O₂ formation via ORR. However, the catalytic sites responsible for WOR in COF systems are often poorly defined, hindering rational catalyst design.¹⁶

Several recent studies have attempted to enhance H₂O₂ production in COF photocatalysts through structural modulation. For example, BTT-PhPD and TTDN-COF systems demonstrated improved catalytic performance through heteroatom engineering that enhances the oxygen reduction reaction ORR pathway.^{13, 17} Nevertheless, these studies primarily focused on promoting ORR activity, while the identification and regulation of WOR active sites were rarely addressed. More recently, COF-N32 suggested that nitrogen atoms may serve as potential catalytic centers for WOR.¹⁸ However, the precise nature of WOR active sites in organic photocatalysts remains controversial. Various structural motifs, including benzene rings, C=C bonds, and C \equiv C bonds, have been proposed as possible WOR centers, yet these assignments are often speculative and lack systematic verification.^{19, 20} Therefore, developing strategies that can precisely define and regulate catalytic active sites for WOR in COF photocatalysts is of great importance.

In parallel, dipole-field engineering has recently emerged as an effective approach for regulating charge separation and transport in conjugated frameworks. By constructing donor-acceptor architectures or introducing asymmetric electronic structures, internal dipole moments can promote charge redistribution and improve photocatalytic performance. For instance, BT-COF achieves accelerated charge transfer through the ordered arrangement of donor-acceptor units, generating both in-plane and intermolecular polarization.²¹ Similarly, BTT-TAA-COF, composed of terthiophene donors and triazine acceptors, exhibits enhanced π -electron delocalization and improved charge mobility.²² Although these approaches effectively enhance charge separation, they mainly rely on long-range intermolecular polarization or framework-level electronic

^a Key Laboratory for Advanced Materials and Institute of Fine Chemicals, School of Chemistry and Molecular Engineering, East China University of Science and Technology, Shanghai, P.R. China. E-mail: fengchen@ecust.edu.cn

Supplementary Information available: [details of any supplementary information available should be included here]. See DOI: 10.1039/x0xx00000x



modulation. In contrast, the influence of localized intramolecular polarization on charge redistribution and catalytic site activation has rarely been explored in COF photocatalysts.

Herein, we report a COF photocatalyst that integrates efficient WOR and ORR sites through an intramolecular local polarization strategy. By incorporating pyrimidine units into the COF framework, the higher electronegativity of nitrogen relative to carbon induces a strongly polarized electronic environment within the molecular unit. Both experimental results and theoretical calculations reveal that the two sp^2 -hybridized nitrogen atoms in the pyrimidine ring serve as highly selective ORR active sites, while the C=C bond polarized by dual nitrogen atoms may serve as a more favorable site for WOR. This localized electronic polarization enables precise regulation of catalytic functionality within a single structural motif. As a result, the resulting TpDa-pyrimidine COF exhibits outstanding photocatalytic performance for sacrificial-agent-free H_2O_2

apparent quantum yield (AQY) of 25.2%, outperforming most reported COF-based photocatalysts. DOI: 10.1039/D6SC00783J

Results and Discussion

Four structurally analogous COFs were synthesized through Schiff base condensation between 1,3,5-triformylphloroglucinol (Tp) and diamines with distinct N-heterocycles, namely 2,4-diamino-1,3,5-triazine (Tz), 4,6-diaminopyrimidine (Da), 2,4-diaminopyridine (Py), and m-phenylenediamine (Ma), yielding TpTz, TpDa, TpPy, and TpMa, respectively (Figure 1a; detailed synthesis protocols are provided in the Supplementary Information). To assess intramolecular local polarization in COFs built from various N-heterocycles, Bader charge analyses were conducted. Figure 1b and 1f show that carbon atoms in nitrogen-free benzene rings display comparable charge transfer amounts, signifying minimal polarization. As the building units evolved from benzene to

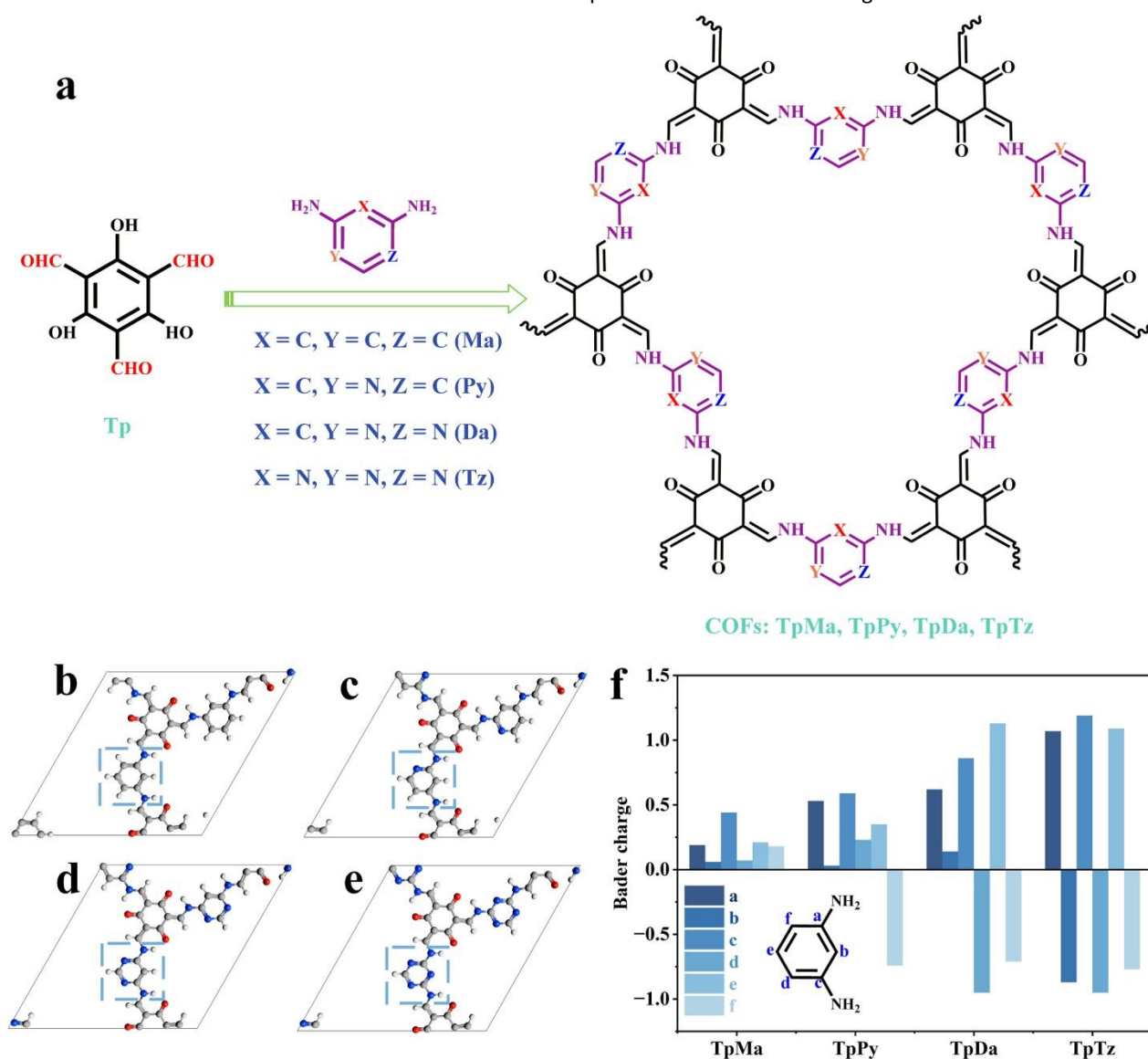


Figure 1 Synthesis and design of COFs featuring intramolecular polarization. (a) COF synthesis scheme. (b-f) Structural snapshots of the four COFs and Bader charge distributions for atoms within the aromatic rings (highlighted by blue dotted boxes) in their respective structures.

production, achieving a rate of 6.94 mmol $g^{-1} h^{-1}$ and an apparent quantum yield (AQY) of 25.2%, outperforming most reported COF-based photocatalysts. pyridine, pyrimidine, and triazine rings, aromatic ring



polarization progressively intensified (Figures 1c-f). Intramolecular polarization tends to enrich electron density on nitrogen atoms while decreasing electron density on carbon atoms, which may contribute to the spatial separation of potential reaction centers.

Structural characterizations were conducted on four as-synthesized COFs. Powder X-ray diffraction (PXRD) analyses (Figures 2a-d) show that all COFs exhibit diffraction peaks for the (100) plane, confirming long-range in-plane order. Intense diffraction peaks at 26°-28° correspond to the (001) plane, indicating the layer-by-layer stacking of 2D structures. Two-dimensional COFs can adopt either eclipsed (AA) or staggered (AB) stacking configurations. Combined structural simulations (Figure S1 and S2) and pore size distribution (Figure S3) analyses indicate that the four COFs adopt the AA stacking mode with pore widths of 1.3-1.6 nm which enables to provide the open channels for mass transport²³. In addition, Pawley refinement of the experimental PXRD data showed good agreement with AA stacking (TpTz: $R_{wp} = 8.26\%$, $R_p = 4.25\%$; TpDa: $R_{wp} = 8.61\%$, $R_p = 7.57\%$; TpPy: $R_{wp} = 2.27\%$, $R_p = 1.79\%$; TpMa: $R_{wp} = 1.76\%$, $R_p = 1.58\%$). N_2 adsorption-desorption isotherms yielded Brunauer-Emmett-Teller (BET) surface areas

of 8.6, 61, 35.1, and 48.2 $m^2 g^{-1}$ for TpTz, TpDa, TpPy and TpMa, respectively.

The FTIR spectra of the COFs and their corresponding monomers are shown in Figure 2f and S4. $-NH_2$ (3300-3460 cm^{-1}) and $-CHO$ (2894 cm^{-1}) peaks²⁴ in diamines and Tp vanished in COFs. Peaks for $C=O$ (1630-1670 cm^{-1}), $C=C$ (1530-1580 cm^{-1}), and $C-N$ (1240-1280 cm^{-1}) emerged²⁵, confirming β -ketoenamine linkage formation. Additional peaks at 1311, 1467, and 1361 cm^{-1} for TpTz, TpDa, and TpPy are assignable to $C=N$ vibrations in triazine, pyrimidine, and pyridine units.^{26, 27} The solid-state ^{13}C NMR spectra of the four COFs display distinct peaks labeled a, b, and c at characteristic chemical shifts assigned to $C=O$ (~180 ppm), $C=C$ (103-105 ppm), and $C-N$ (144 ppm), respectively.²⁸ This observation correlates well with FTIR data, providing evidence for the formation of the β -ketoenamine linkage. Carbon signals from the phenyl rings primarily appear in the lower chemical shift region (112-135 ppm). In contrast, the ^{13}C signals associated with the nitrogen-containing heterocyclic rings exhibit shifts towards higher chemical shifts (143-160 ppm). This phenomenon arises from the influence of the highly electronegative nitrogen atoms and

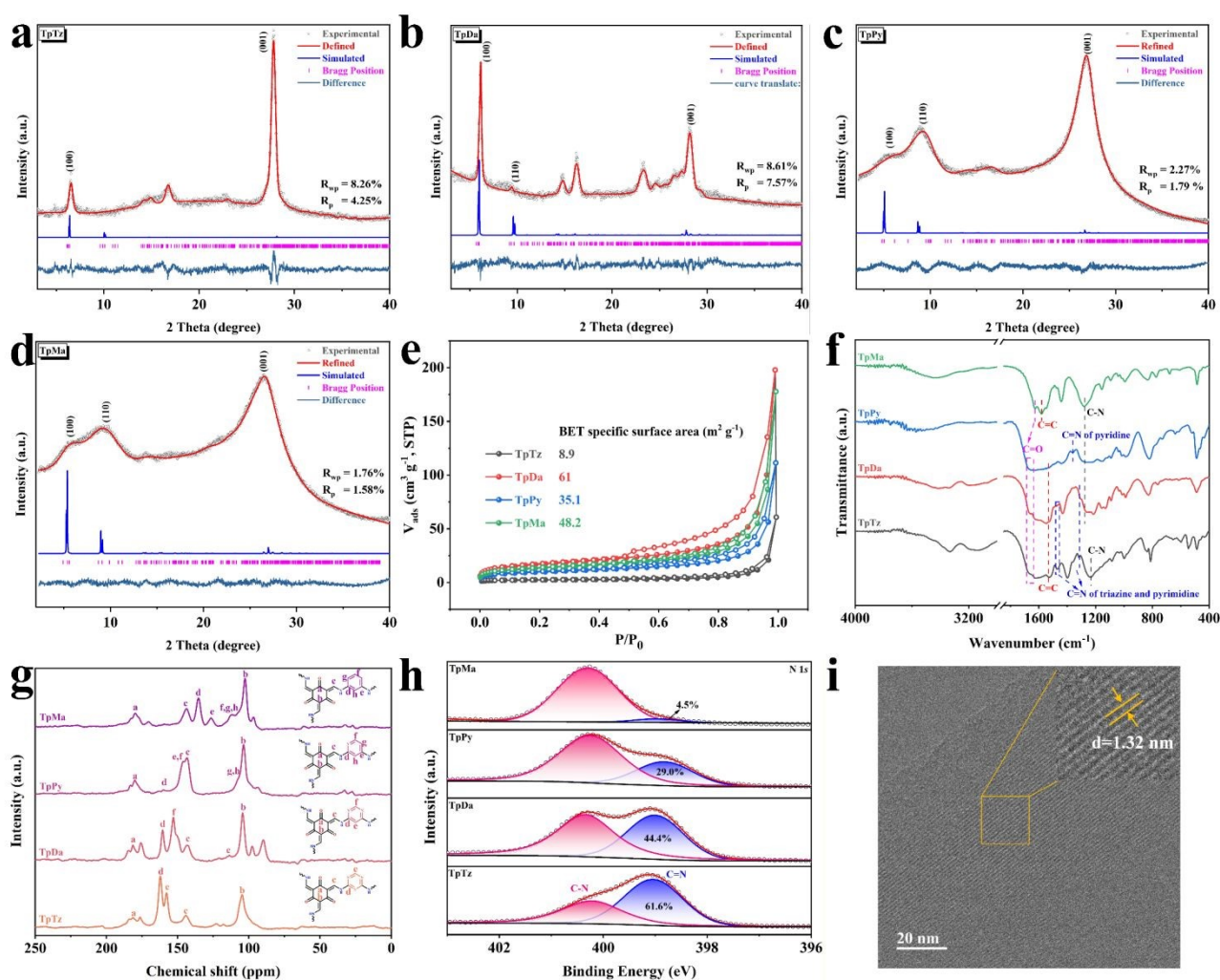


Figure 2 Structural characterization of COF structures. (a-d) Simulated and experimental PXRD curves and structures of TpTz, TpDa, TpPy and TpMa. (e) N_2 adsorption-desorption (77K) of COFs. (f) FTIR spectra of COFs. (g) ^{13}C NMR spectra of COFs. (h) XPS spectra of N 1s in COFs. (i) HRTEM images of TpDa.



reflects the intramolecular polarization effect inherent to these asymmetric heterocyclic units.

The XPS survey spectra (Figure S5a) confirm the presence of C, N, and O in all COFs. Notably, the C 1s peak intensity progressively increases across the series TpTz < TpDa < TpPy < TpMa, while the N 1s intensity decreases accordingly. This inverse correlation directly corresponds to the carbon/nitrogen content ratio in the diamine monomers. Deconvolution of the high-resolution N 1s XPS spectra (Figure 2h) reveals two peaks at 398.9 eV and 400.3 eV, assigned to C=N and C-N species, respectively.²⁹ The relative area of the C=N peak sequentially decreases from TpTz to TpMa, with quantified proportions of 61.6%, 44.4%, 29.0%, and 4.5%, respectively. The minor C=N component in TpMa originates from ketoenamine-to-enolimine tautomerization. Elemental analysis (EA, Table S1) further corroborates the compositional trend observed by XPS (Table S2), with both techniques reflecting the monomeric C/N ratios. The high-resolution O 1s spectra (Figure S5b) exhibit two components at ~531 eV and ~533 eV, attributed to C=O and C-O groups.³⁰ Collectively, FT-IR, ¹³C NMR, and XPS results confirm the successful synthesis of four COFs featuring the β -ketoenamine linkage.

Scanning electron microscopy (SEM) images (Figure S6) reveal the morphology of the synthesized COFs. A distinct

morphological evolution from nanorods to webbed networks is observed with decreasing nitrogen content. TpTz and TpDa comprise stacked nanorods several hundred nanometers in length and 60-80 nm in diameter. In contrast, TpPy and TpMa exhibit an interconnected webbed structure formed by numerous fibrils approximately 30 nm in diameter. High-resolution transmission electron microscopy (HRTEM) of TpDa (Figure 2i) clearly shows lattice fringes with a measured interplanar spacing of 1.32 nm. These fringes are assigned to the (100) crystallographic plane, providing more definitive evidence for the crystalline structure of TpDa.

To elucidate the structure-activity relationships in photocatalytic H₂O₂ production, we systematically evaluated the optical and charge separation properties of the four COFs. Ultraviolet-visible diffuse reflectance spectroscopy (UV-Vis DRS, Figure 3a) reveals absorption edges extending to ~600 nm for all COFs, attributed to their highly conjugated frameworks. Tauc plot analysis (Figure 3b) yields optical band gaps (E_g) of 2.49 eV (TpTz), 2.46 eV (TpDa), 2.34 eV (TpPy), and 2.43 eV (TpMa). XPS valence band (VB) spectra (Figure S7) determine valence band maxima (VBM) at 2.26 V (TpTz), 1.89 V (TpDa), 1.95 V (TpPy), and 1.87 V (TpMa) relative to the NHE. The conduction band minimum (CBM) was subsequently calculated from E_g and VBM. The resultant energy band structures (Figure 3c) demonstrate

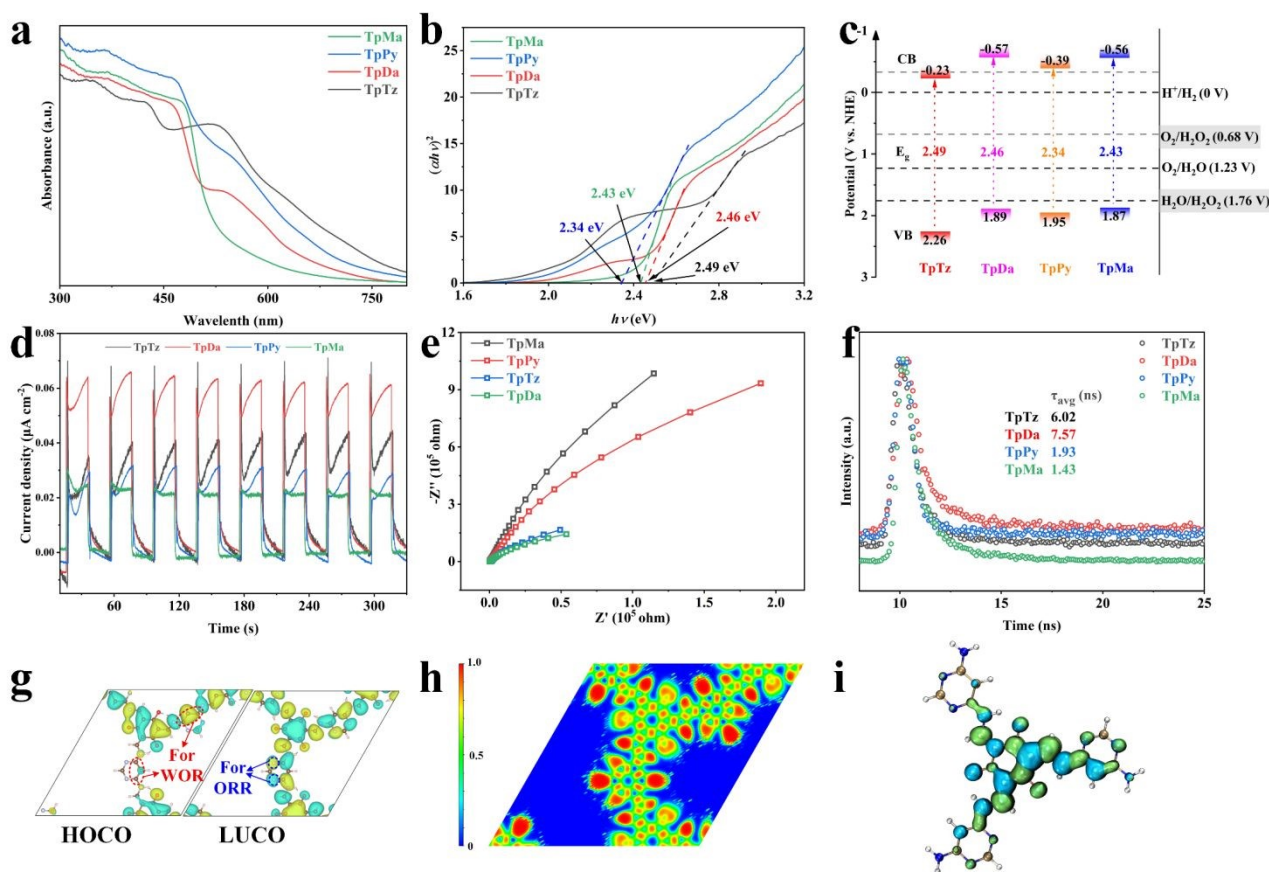


Figure 3 Optical property characterization and charge separation of COFs. (a) Solid-state UV-vis diffuse reflectance spectra and (b) Tauc plots for bandgaps calculation. (c) Band-structure diagrams of COFs (all redox potentials referenced to NHE at pH = 0). (d) Photocurrent density of COFs. (e) EIS curves of COFs. (f) Time-resolved photoluminescence spectroscopy spectra of COFs. (g) HOCO and LUCO distribution of TpDa. (h) The calculated Electron Localization Function (ELF) diagrams of TpDa. Red and blue represent complete localization and complete delocalization of electrons, respectively. (i) Distribution of holes (blue) and electrons (green) in TpDa obtained through TD-DFT calculations (Isosurface value = 0.001).



that for all COFs, the CBM is strictly more negative than the O_2/H_2O_2 redox potential (0.695 V vs. NHE), while the VBM is more positive than the O_2/H_2O redox potential (1.23 V vs. NHE). These thermodynamic relationships suggest that photogenerated electrons can drive the reduction of O_2 to H_2O_2 , while the holes possess sufficient driving force to promote WOR. Notably, the four COFs exhibit no significant differences in their band structures, suggesting that their photocatalytic performance is predominantly governed by the nature of the active sites.

Photoelectrochemical measurements reveal that TpDa generates a higher photocurrent density compared to TpTz, TpPy, and TpMa (Figure 3d), indicating superior charge separation efficiency, which facilitates interfacial redox reactions. Electrochemical impedance spectroscopy (EIS) analysis demonstrates a significantly lower charge transfer resistance for TpDa and TpTz relative to TpMa and TpPy (Figure 3e), confirming that interfacial charge mobility markedly improves with increased intramolecular polarization. Time-resolved photoluminescence studies show average fluorescence lifetimes of 6.02 ns (TpTz), 7.57 ns (TpDa), 1.93 ns (TpPy), and 1.43 ns (TpMa) (Figure 3f and Table S3). Notably, TpDa and TpTz exhibit considerably prolonged lifetimes, ascribed to polarization of nitrogen-containing heterocycles enhancing charge carrier separation. Intriguingly, although TpTz exhibits stronger calculated polarization, its photocurrent response, EIS behavior, and average fluorescence lifetime are slightly inferior to those of TpDa. A quantitative analysis of the (100) diffraction peaks in the PXRD patterns shows that the full width at half maximum (FWHM) of TpTz (0.363) is larger than that of TpDa (0.278) (Figure 2a,b), indicating a lower degree of in-plane ordering. The higher in-plane ordering of TpDa may facilitate more efficient charge carrier separation, which could contribute to its improved photoelectrochemical performance. Subsequently, we conducted density functional theory (DFT) calculations utilizing full periodic models rather than repeated monomeric fragments, enabling more accurate representation of the highest occupied crystalline orbital (HOCO) and lowest unoccupied crystalline orbital (LUCO) distributions³¹ in the synthesized crystalline porous materials. As illustrated in Figure 3g, no discernible separation between HOCO and LUCO occurs in the keto-enamine region of TpDa. However, periodic separation emerges within the polarized pyrimidine ring. Specifically, LUCO is predominantly localized on the two nitrogen heteroatoms, while HOCO is chiefly distributed across C=C bonds. Consequently, upon photoexcitation, electrons and holes are spatially separated at N sites and C=C bonds within the pyrimidine ring, which is consistent with the possibility that N sites participate in ORR while C=C bonds may be involved in WOR. For TpTz, pronounced in-plane periodic separation of HOCO and LUCO is evident: LUCO concentrates on N atoms within the triazine ring, and HOCO resides within the keto-enamine moiety (Figure S8a). Given the absence of C=C bonds in the triazine ring, WOR predominantly occurs at the keto-enamine C=C sites. Compared to TpDa and TpTz, TpPy and TpMa exhibit negligible HOCO-LUCO periodic separation due to insufficient intramolecular polarization in their pyridine and

benzene rings (Figure S8b and S8c). Additionally, we computed electron localization function (ELF) maps for all four COFs (Figure 3h and S9). Notably, relative to the fully localized electrons at carbon atoms in benzene rings, nitrogen atoms in N-heterocycles display enhanced electron delocalization, which may contribute to improved catalytic activity. Further, time-dependent density functional theory (TDDFT) calculations mapped the distributions of excited-state electrons and holes^{32, 33} in molecular fragments of the COFs (Figure 3i and S10). TDDFT reveals that in N-heterocyclic units of TpTz, TpDa, and TpPy, electrons localize on N atoms while holes remain at C=C bonds. Conversely, in TpMa, which lacks this heterocyclic cycle, electrons and holes are partially delocalized in ketoamine and benzene sections, respectively. This suggests that polarized N-heterocycles may enhance spatial carrier separation^{21, 34} and potentially provide favorable sites for ORR and WOR.

The photocatalytic H_2O_2 synthesis performance of the four COFs were evaluated under xenon lamp irradiation. TpDa exhibited a H_2O_2 production rate of 6.94 mmol g⁻¹ h⁻¹ in pure water under O_2 atmosphere (Figure 4a), far exceeding those of TpPy (2.18 mmol g⁻¹ h⁻¹), TpTz (1.28 mmol g⁻¹ h⁻¹), and TpMa (0.22 mmol g⁻¹ h⁻¹). A distinct parabolic trend is observed in the H_2O_2 photosynthetic efficiency as a function of nitrogen content, which initially increases and subsequently decreases with increasing nitrogen incorporation. In contrast, the non-heterocyclic COF TpMa exhibits negligible photocatalytic activity. This indicates that H_2O_2 photosynthesis performance is not solely determined by the number of nitrogen atoms, but also by the structural nature of the heteroaromatic units. H_2O_2 decomposition capabilities under Ar atmosphere were subsequently tested (Figure 4b). Without sacrificial agents, COF decomposition activity directly correlates with their H_2O_2 production rates. No noticeable H_2O_2 decomposition was observed under dark conditions (Figure S11a). This confirms that the H_2O_2 decomposition observed in Figure 4b mainly originates from photocatalytic processes. However, adding the electron scavenger NaIO₃ completely suppressed H_2O_2 decomposition for all COFs (Figure S11b), confirming that photogenerated electrons drive decomposition. The enhanced decomposition kinetics of TpDa, which have similar reduction sites and potentials to other COFs, further corroborates its superior charge separation capability. During prolonged operation, TpDa steadily produced H_2O_2 at the fastest speed, but as the concentration of H_2O_2 increased, the rate of H_2O_2 production gradually decreased, which was attributed to the high concentration of H_2O_2 competing for oxygen reduction active sites (Figure 4c). Subsequently, we evaluated the effect of TpDa dosage on the production rate of H_2O_2 . Catalyst dosage optimization revealed increasing H_2O_2 production rates with TpDa concentration, plateauing at 0.33 g L⁻¹ with negligible further increase (Figure S12). This optimal dosage was selected for subsequent apparent quantum yield (AQY) and solar-to-chemical conversion (SCC) efficiency measurements. TpDa achieved an AQY of 25.2% at 400 nm (Figure 4d), exhibiting strong spectral dependency, along with a remarkable SCC efficiency of 0.54%. These values surpass most state-of-the-art COF photocatalysts (Figure 4e and Table S4). After five catalytic



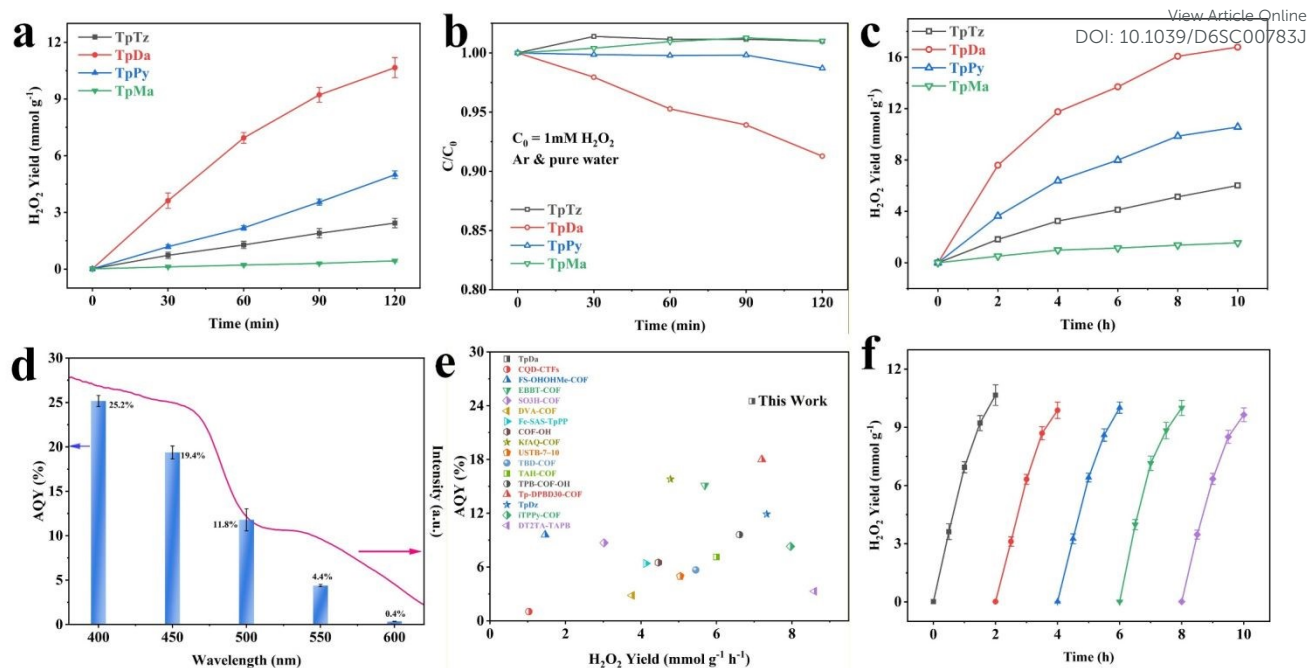


Figure 4 H₂O₂ photosynthesis of COFs. (a) Photocatalytic activity of COFs for H₂O₂ production under the irradiation of xenon light in pure water. Error bars on mean values are standard deviations of three independent H₂O₂ production tests. (b) Photocatalytic decomposition of H₂O₂ (C₀ = 1 mM) in pure water under Ar atmosphere over COFs. (c) Photocatalytic H₂O₂ production of COFs for 10 h. (d) Wavelength-dependent testing of apparent quantum efficiency (AQY). Error bars on mean values are standard deviations of three independent H₂O₂ production tests. (e) Photocatalytic H₂O₂ production rate and AQY for TpDa in comparison with previously reported COF-based photocatalysts. (f) Cyclic stability measurement of TpDa for H₂O₂ generation. Error bars on mean values are standard deviations of three independent H₂O₂ production tests.

cycles, all COFs retained >90% initial activity (**Figure 4f**). Post-cycling characterization revealed decreased TpDa crystallinity (**Figure S13**) while maintaining chemical composition (FTIR: **Figure S14**; XPS: **Figure S15**), demonstrating robust chemical stability. Furthermore, decomposition temperatures exceeding 300°C indicate substantial thermal resilience (**Figure S16**).

The photocatalytic H₂O₂ formation mechanism comprises two half-reactions: two-electron oxygen reduction (2e⁻ ORR) and two-electron water oxidation (2e⁻ WOR).^{35, 36} In most photocatalytic systems, the 2e⁻ ORR pathway (Equation 1) is favored over the 2e⁻ WOR route (Equation 2).³⁷ Water oxidation predominantly follows the thermodynamically preferred four-electron pathway (4e⁻ WOR, Equation 3).³⁸ However, its sluggish four-electron transfer kinetics frequently renders 4e⁻ WOR the rate-limiting step in the overall H₂O₂ synthesis process.³⁹



To elucidate the mechanism of cathodic ORR in the COFs, linear sweep voltammetry (LSV) curves were acquired using a rotating ring-disk electrode (RRDE) (**Figure S17**). The RRDE measurements were performed in O₂-saturated phosphate buffer electrolyte under neutral pH conditions in order to approximate the photocatalytic reaction environment as closely as possible. The electron transfer numbers (n) calculated for TpTz, TpDa, TpPy, and TpMa were 2.45, 2.54, 2.55, and 2.63, respectively, approaching a value of 2. These values suggest that the ORR proceeds predominantly through a two-electron pathway, although minor contributions from other pathways cannot be excluded. The corresponding H₂O₂ selectivities are

77.6%, 72.8%, 72.6%, and 68.5%, respectively (**Figure S18**).

These results suggest that ORR over the COFs mainly follows a 2e⁻ pathway, providing favorable selectivity toward H₂O₂ formation. The RRDE results mainly serve as supporting evidence for the feasibility of the 2e⁻ ORR pathway, while the photocatalytic mechanism is primarily inferred from photocatalytic control experiments and radical trapping studies. To validate this mechanism, a series of control experiments were designed by modulating the photocatalytic reaction environment. As shown in **Figure 5a**, introduction of the electron scavenger NaIO₃ drastically suppressed H₂O₂ yield. Subsequent Ar purging (in the presence of NaIO₃) abolished H₂O₂ detection, demonstrating that H₂O₂ originates exclusively from photogenerated electron-mediated O₂ reduction rather than WOR. Addition of nitroblue tetrazolium (NBT), a superoxide ([•]O₂⁻) scavenger, to the reaction system resulted in a sharp decline in H₂O₂ content. This observation substantiates a stepwise 2e⁻ ORR mechanism, where O₂ undergoes initial single-electron reduction to superoxide/hydroperoxyl radicals ([•]O₂⁻/HOO[•]), followed by further reduction to H₂O₂.

Correspondingly, to validate the impact of WOR on H₂O₂ generation, EDTA-2Na was employed as a valence band hole scavenger. This intervention enhanced the H₂O₂ production performance of TpTz, TpDa, and TpPy by factors of 2.82, 1.30, and 1.90, respectively (TpMa was excluded from comparison due to its poor performance resulting from the lack of high-activity ORR sites). Scavenging holes accelerated the oxidation half-reaction kinetics, thereby promoting the H₂O₂ generation rate via ORR. Notably, TpTz exhibited the most significant performance enhancement, while TpDa showed the smallest



improvement. It indicates that the H_2O_2 production efficiency of TpTz is more strongly influenced by WOR kinetics, followed by TpPy, and least affected for TpDa. This trend may arise because the polarized pyrimidine and pyridine rings in TpDa and TpPy offer additional potential sites (C=C) for WOR. In contrast, while the triazine ring in TpTz offers abundant ORR sites (Pyridine nitrogen), it lacks activated sites conducive to efficient WOR. Furthermore, using tert-butanol (tBA) as a hydroxyl radical ($\cdot\text{OH}$) scavenger led to increased H_2O_2 production for TpTz and TpPy but yielded a paradoxical decrease for TpDa. This divergence suggests that TpDa possesses a strong inherent capability for oxidizing $\cdot\text{OH}$ intermediates. Consequently, adding tBA competes for catalytic surface sites, hindering further anodic oxidation processes. Conversely, TpTz and TpPy exhibit weaker $\cdot\text{OH}$ oxidation capacity; thus, tBA addition scavenges $\cdot\text{OH}$ radicals, allowing the catalytic cycle to bypass energetically unfavorable sequential oxidation steps. To verify this hypothesis, electron paramagnetic resonance (EPR) spectroscopy was employed using NaIO_3 as an electron scavenger to detect $\cdot\text{OH}$ radicals. (Note: $\text{DMPO}\cdot\text{O}_2^-$ adducts readily convert to $\text{DMPO}\cdot\text{OH}$ in aqueous environments⁴⁰). As

shown in **Figure 5b**, TpDa generated the lowest detectable $\cdot\text{OH}$ signal during photocatalysis, indicating its high efficiency in rapidly converting $\cdot\text{OH}$ intermediates formed on its surface. This observation aligns perfectly with the inferences drawn from the tBA scavenger experiments in **Figure 5a**. Additionally, EPR revealed similar $\text{DMPO}\cdot\text{O}_2^-$ signal intensities for TpTz, TpDa, and TpPy but a substantially higher signal for TpMa (**Figure S19**). This apparent discrepancy with the performance metrics (where TpMa performs poorly) will be addressed in the subsequent theoretical calculation section on reaction pathways.

Sacrificial agent experiments confirm that COF-based photoanodes are incapable of generating H_2O_2 via the WOR, thus restricting anodic products to O_2 . We evaluated the O_2 evolution capabilities of the four COFs using gas chromatography. As shown in **Figure 5c**, TpDa exhibits superior oxygen evolution activity, suggesting that strong local polarization may activate more favorable sites for WOR. To further probe the relationship between WOR and ORR, we adopted an alternative quantitative strategy using a low concentration of Ag^+ (0.1 mM) as an electron acceptor under

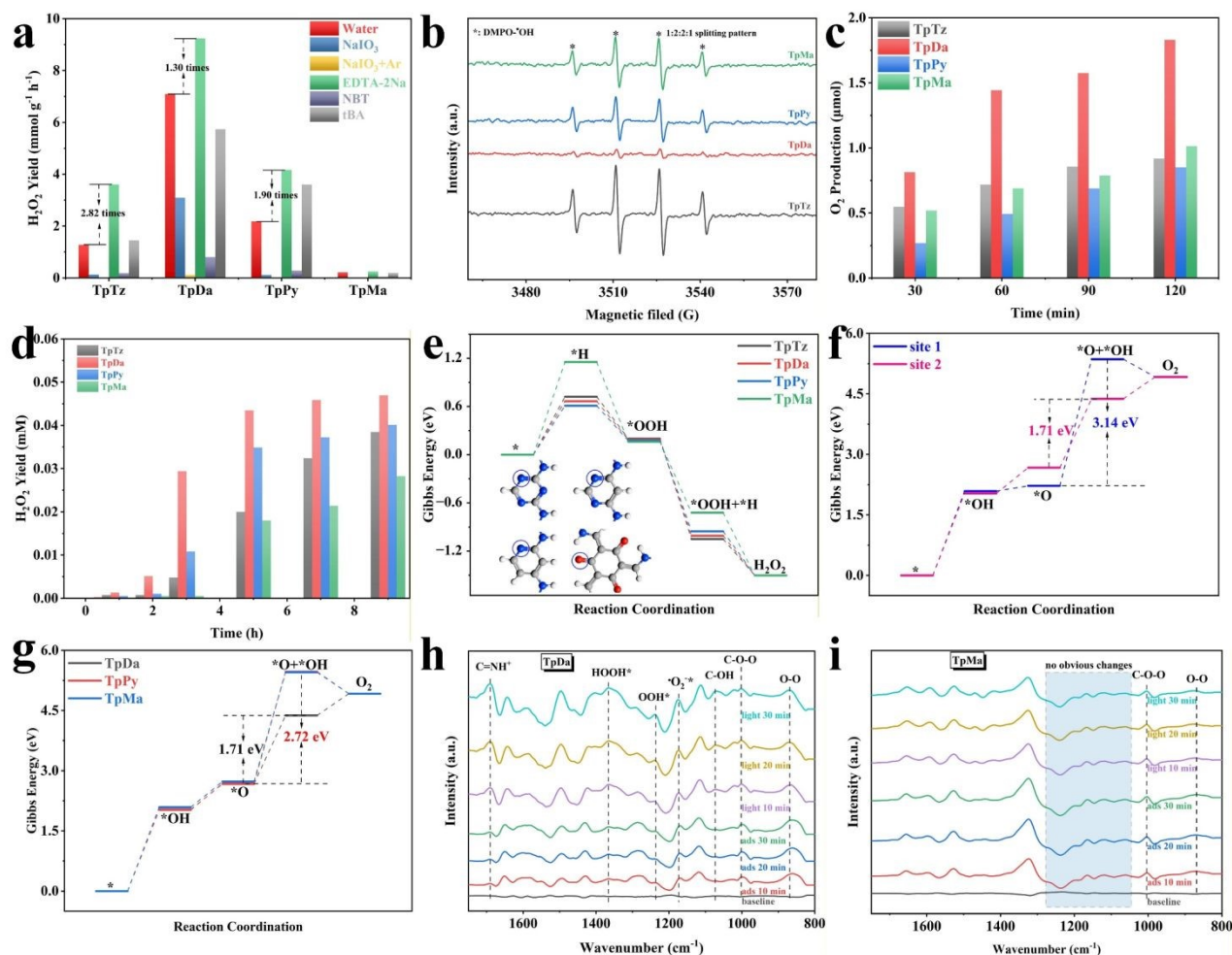


Figure 5 Reaction pathways and mechanisms. (a) Photocatalytic H_2O_2 production rate of COFs with different atmospheres. (b) EPR profiles with DMPO for $\cdot\text{OH}$ trapping and NaIO_3 (20 mM) as electron acceptor based on COFs after 5 min irradiation of visible light. (c) Amount of O_2 produced on COFs in NaIO_3 (20 mM). (d) Photocatalytic H_2O_2 production with electron acceptor (0.1 mM AgNO_3) under Ar atmosphere. (e) Gibbs free energy diagrams of COFs for H_2O_2 photogeneration by ORR. (f) Gibbs free energy diagrams for $4e^-$ WOR at different sites based on TpDa. (g) Gibbs free energy diagrams for $4e^-$ WOR at site2 based on TpDa, TpPy and TpMa. In situ DRIFT spectra of (h) TpDa and (i) TpMa.

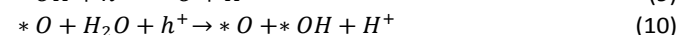


O₂-free conditions. In this configuration, H₂O₂ can only be produced via the reduction of O₂ generated from water oxidation. As shown in **Figure 5d**, negligible H₂O₂ was detected during the first hour for all four COFs, indicating that photogenerated electrons were primarily consumed by Ag⁺ reduction. In the second hour, TpDa began to show a clear H₂O₂ signal, whereas the three comparison samples exhibited much weaker signals. This suggests that TpDa possesses faster WOR kinetics, which accelerates the consumption of Ag⁺ and allows the system to enter the ORR-driven H₂O₂ formation stage earlier. Subsequently, the H₂O₂ concentration gradually increased for all samples. Notably, the H₂O₂ concentration for TpDa quickly approached a stable value of approximately 0.046 mM, corresponding to about 92% of the theoretical value (0.05 mM). The remaining ~8% loss may arise from the reaction equilibrium of H₂O₂ formation. This behavior indicates that the O₂ generated from WOR in the TpDa system was rapidly consumed by ORR, whereas the comparison samples continued to generate O₂ more slowly.

To gain deeper mechanistic insights into the COF photocatalysts in this study, density functional theory (DFT) calculations were employed to investigate the reaction pathways for both 2e⁻ ORR and 4e⁻ WOR. In 2e⁻ ORR, the initial step typically involves adsorption activation of either O₂ or H⁺. The pivotal role of nitrogen atoms in heterocyclic rings was probed by comparing adsorption free energies (ΔG_{ads}) for O₂ and H⁺ between TpDa (with N-heterocycles) and TpMa (without N-heterocycles). Results revealed that TpMa exhibited a 0.27 eV lower ΔG_{ads} for O₂ than for H⁺, favoring O₂ adsorption activation (Equation 4) (**Figure S20**). Conversely, TpDa showed a 0.21 eV lower ΔG_{ads} for H⁺ activation than for O₂, indicating preferential H⁺ adsorption (Equation 5) (**Figure S21**). The preferential O₂ activation to form *O₂⁻ by TpMa likely explains its intensified DMPO-*O₂⁻ EPR signal in **Figure S19**. Using proton activation (*H formation) as the initial step, the full 2e⁻ ORR pathway was computed. Optimized structural snapshots (**Figures S22-25**) show that in the second step, O₂ adsorbs on the β -ketoenamine chain's C=C bond and reacts with *H to form *OOH (Equation 6). Subsequently, the second H⁺ adsorbs on C=O and hydrogen-bonds with *OOH to form *HOOH (Equation 7), which ultimately desorbs as H₂O₂. Complete free energy diagrams for 2e⁻ ORR across all four COFs are presented in **Figure 5e**. TpTz, TpDa, and TpPy (N-heterocycle-containing) display similar free energy profiles, with substantially lower energy barriers for the *H and *OOH+*H intermediates compared to TpMa, demonstrating the catalytic enhancement from heterocyclic N atoms. Moreover, increased pyridinic-N sites stabilize *H and *OOH intermediates via additional adsorption centers, thereby optimizing 2e⁻ ORR efficiency. Despite possessing the highest pyridinic-N content, TpTz exhibits lower photocatalytic activity, which may be associated with kinetic limitations related to the anodic WOR process.



In the 4e⁻ WOR process, DFT calculations revealed that all four COFs exhibit identical reaction mechanisms, as detailed in **Figures S26-32**. In the initial step, a single H₂O molecule dissociates on the C=C bond to generate hydroxyl radical adsorbate (Equation 8). In the second step, *OH undergoes dehydrogenation to form the epoxy intermediate *O (Equation 9). The third step involves dissociation of another H₂O molecule, yielding the *O + *OH co-adsorbed state (Equation 10). This co-adsorbed state subsequently oxidizes in the fourth step to form O₂ (Equation 11). Notably, TpDa, TpPy, and TpMa (but not TpTz) possess two distinct WOR active sites: the C=C bond of β -ketoenamine chain (site1) and C=C bond of aromatic ring (site2). Free energy diagrams from DFT indicate that the formation of the *O + *OH intermediate represents the rate-limiting step in 4e⁻ WOR, with $\Delta G \geq 2.99$ eV (**Figure 5f**; **Figure S33** and **S34**). The 4e⁻ WOR on site1 of the four COFs showed a close trend (**Figure S35**). Across all four COFs, the ΔG for *O + *OH formation is consistently lower on site2 than on site1, establishing site2 as the primary reaction site for 4e⁻ WOR. ΔG on site2 of TpDa is markedly lower (1.71 eV), compared to 2.72 eV for TpMa and 2.79 eV for TpPy (**Figure 5g**). This suggests that strong polarization from bipyridine nitrogen atoms can lower the thermodynamic barrier for WOR at site2. The lowered barrier may accelerate the conversion of *OH to downstream intermediates, which could contribute to improved overall H₂O₂ synthesis. Concurrently, this mechanistic insight explains the minimal DMPO-*OH signal observed for TpDa in **Figure 5b**, as rapid *OH turnover reduces DMPO trapping efficiency.



Subsequent in situ diffuse reflectance infrared Fourier transform spectroscopy (DRIFTS) validated the DFT-derived catalytic mechanism. Upon irradiation, peaks assignable to C=NH⁺ species (~1692 cm⁻¹)⁴¹ emerged in DRIFTS spectra of TpTz (**Figure S36**), TpDa (**Figure 5h**), and TpPy (**Figure S37**), with intensity increasing progressively over illumination time. This feature was absent in pyridine-N-free TpMa (**Figure 5i**), confirming proton adsorption activation on pyridinic nitrogen as the initial ORR step in N-heterocyclic COFs, consistent with DFT predictions. Peaks at 1173, 1237, and 1365 cm⁻¹ correspond to O-O stretching modes of adsorbed *O₂⁻, OOH, and HOOH* intermediates, respectively.^{42, 43} Crucially, TpDa exhibited substantially stronger intensities for all three oxygen-related species than TpTz, TpPy, and TpMa, indicating accelerated ORR kinetics. This enhancement stems from the reduced thermodynamic barrier in WOR (previously limiting overall H₂O₂ synthesis). Furthermore, the 1073 cm⁻¹ peak in DRIFT spectra is attributed to C-OH species.¹⁹ As *OH is a critical intermediate in 4e⁻ WOR, C-OH formation confirms water oxidation occurs on C=C bonds. The strongest C-OH signal in TpDa suggests more favorable WOR activity, specifically the C=C bonds activated by strong polarization from bipyridinic nitrogen atoms. Collectively, these results are consistent with the reaction pathways suggested by the DFT calculations. The data demonstrates that strong polarization within nitrogen



heterocycles plays a crucial promotional role in both ORR and WOR processes.

Conclusions

This work demonstrates a novel strategy to enhance the photocatalytic performance of COFs through local polarization engineering. By precisely tuning intramolecular polarization, carrier separation is optimized and favorable WOR sites are activated, which helps facilitate the overall H₂O₂ production process. Among the synthesized COFs, the pyrimidine-based TpDa exhibits outstanding sacrificial-agent-free activity, achieving an H₂O₂ production rate of 6.94 mmol g⁻¹ h⁻¹ and an apparent quantum efficiency of 25.2% under ambient conditions. In situ DRIFTS analysis combined with DFT calculations showed that the strongly polarized nitrogen heterocyclic reduced the energy barrier associated with WOR on the C=C bond while providing highly active ORR sites (pyridine nitrogen). These findings highlight the important role of local polarization in influencing photocatalytic reactions and establish a rational design principle for the development of advanced COF-based materials for solar-driven chemical conversions.

Author contributions

Donghui Wang: Writing – original draft, Methodology, Investigation, Formal analysis, Data curation, Visualization, Software. Jin-Gang-Lu Tao: Investigation, Software, Formal analysis. Haiyang Zhang: Data curation, Investigation, Formal analysis. Po Zhang: Investigation, Software, Formal analysis. Feng Chen: Writing – review & editing, Investigation, Funding acquisition, Formal analysis, Conceptualization.

Conflicts of interest

There are no conflicts to declare.

Data availability

The data that support the findings of this study are available from the corresponding author upon reasonable request.

Acknowledgements

This work was supported by National Key R&D Program of China No.2024YFA1211004. Additional support was provided by the Feringa Nobel Prize Scientist Joint Research Center at East China University of Science and Technology.

Notes and references

1. C. Shao, X. Yu, Y. Ji, J. Xu, Y. Yan, Y. Hu, Y. Li, W. Huang and Y. Li, Perfluoroalkyl-modified covalent organic frameworks for continuous photocatalytic hydrogen peroxide synthesis and

extraction in a biphasic fluid system, *Nat. Commun.*, 2024, **15**, 8023. DOI: 10.1039/D6SC00783J

- J. Zhang, F. Xue and Z. Wang, Terpyridine- and Quarterpyridine-Based Cationic Covalent Organic Frameworks for Visible-Light-Catalytic H₂O₂ Synthesis, *Angew. Chem. Int. Ed.*, 2025, **64**, e202425617.
- X. Li, G. Zhang, N. Li, Q. Xu, H. Li, J. Lu and D. Chen, Self-Floating Photocatalytic System for Highly Efficient Hydrogen Peroxide Production and Organic Synthesis on Carbon Dots Decorated Conjugated Microporous Polymer, *Adv. Funct. Mater.*, 2024, **34**, 2316773.
- W. Yu, F. Chen, X. Zhang, N. Tian, N. Zhang, Y. Zhang and H. Huang, Dipole field and locally polarized electric field in asymmetric crystalline carbon nitride for high-efficiency artificial photosynthesis of hydrogen peroxide, *Nano Energy*, 2025, **138**, 110862.
- X. Zhang, S. Cheng, C. Chen, X. Wen, J. Miao, B. Zhou, M. Long and L. Zhang, Keto-anthraquinone covalent organic framework for H₂O₂ photosynthesis with oxygen and alkaline water, *Nat. Commun.*, 2024, **15**, 2649.
- X. Zhang, H. Su, P. Cui, Y. Cao, Z. Teng, Q. Zhang, Y. Wang, Y. Feng, R. Feng, J. Hou, X. Zhou, P. Ma, H. Hu, K. Wang, C. Wang, L. Gan, Y. Zhao, Q. Liu, T. Zhang and K. Zheng, Developing Ni single-atom sites in carbon nitride for efficient photocatalytic H₂O₂ production, *Nat. Commun.*, 2023, **14**, 7115.
- H. Chai, J. Nan, W. Jin, F. Wu, B. Liu and Y. Guo, Zinc phthalocyanine/polymer carbon nitride S-scheme heterojunction with internal electric field and near-infrared absorption for photocatalytic H₂O₂ production, *Chem. Eng. J.*, 2024, **489**, 151293.
- D. Liu, C. Zhang, J. Shi, L. Li, W. Liu, M. Liu, J. Su, J. Liu and L. Guo, Constructing asymmetric dual active sites of Ag single atoms and nitrogen defects on carbon nitride for enhanced photocatalytic H₂O₂ production, *Journal of Materials Science & Technology*, 2025, **223**, 56-65.
- F. Sun, Y. Luo, S. Kuang, M. Zhou, W.-K. Ho and H. Tang, Ultraviolet-visible-near-infrared light responsive inorganic/organic S-scheme heterojunctions for efficient H₂O₂ production, *Journal of Materials Science & Technology*, 2025, **229**, 287-295.
- Y. Luo, X. Wang, P. Wang, F. Chen and H. Yu, Inorganic/organic hybrid interfacial internal electric field modulated charge separation of resorcinol-formaldehyde resin for boosting photocatalytic H₂O₂ production, *Chem. Eng. J.*, 2024, **497**, 154886.
- F. Zhang, X. Lv, H. Wang, J. Cai, H. Wang, S. Bi, R. Wei, C. Yang, G. Zheng and Q. Han, p- π Conjugated Covalent Organic Frameworks Expedite Molecular Triplet Excitons for H₂O₂ Production Coupled with Biomass Upgrading, *Adv. Mater.*, 2025, **37**, 2502220.
- J. Hao, Y. Tang, J. Qu, Y. Cai, X. Yang and J. Hu, Robust Covalent Organic Frameworks for Photosynthesis of H₂O₂: Advancements, Challenges and Strategies, *Small*, 2024, **20**, 2404139.
- C. Wu, F. Chu, Y. Hao, X. Li, X. Jia, Y. Sun, J. Gu, P. Jia, A. Wang and J. Jiang, Dual O₂ reduction centers of COFs boosting H₂O₂ photosynthesis, *Chin. J. Catal.*, 2025, **74**, 329-340.
- Y. Yang, X. Chu, H.-Y. Zhang, R. Zhang, Y.-H. Liu, F.-M. Zhang, M. Lu, Z.-D. Yang and Y.-Q. Lan, Engineering β -ketoamine covalent organic frameworks for photocatalytic overall water splitting, *Nat. Commun.*, 2023, **14**, 593.
- J.-Y. Yue, Z.-X. Pan, Y. Guo, P. Yang and B. Tang, Distinct oxygen reduction pathways for solar H₂O₂ production by regulating



- unsaturated bonds in covalent organic frameworks, *Chem. Sci.*, 2025, **16**, 13883-13892.
16. C. Sun, Y. Han, H. Guo, R. Zhao, Y. Liu, Z. Lin, Z. Xiao, Z. Sun, M. Luo and S. Guo, Proton Reservoir in Covalent Organic Framework Compensating Oxygen Reduction Reaction Enhances Hydrogen Peroxide Photosynthesis, *Adv. Mater.*, 2025, **37**, 2502990.
 17. Q. Nan, J. Ning, B. Han, H. Wei, X. Wang, Y.-Y. Gu, S. Zhou, G. Cao, G. Zhang, X. Li, Y. Jia and L. Hao, Boosting the photocatalytic H₂O₂ production of covalent organic frameworks with a heteroatom-locked acceptor and gas diffusion system, *Chem. Sci.*, 2026, **17**, 466-474.
 18. F. Liu, P. Zhou, Y. Hou, H. Tan, Y. Liang, J. Liang, Q. Zhang, S. Guo, M. Tong and J. Ni, Covalent organic frameworks for direct photosynthesis of hydrogen peroxide from water, air and sunlight, *Nat. Commun.*, 2023, **14**, 4344.
 19. Y. Huang, M. Shen, H. Yan, Y. He, J. Xu, F. Zhu, X. Yang, Y.-X. Ye and G. Ouyang, Achieving a solar-to-chemical efficiency of 3.6% in ambient conditions by inhibiting interlayer charges transport, *Nat. Commun.*, 2024, **15**, 5406.
 20. L. Zhang, C. Wang, Q. Jiang, P. Lyu and Y. Xu, Structurally Locked High-Crystalline Covalent Triazine Frameworks Enable Remarkable Overall Photosynthesis of Hydrogen Peroxide, *Journal of the American Chemical Society*, 2024, **146**, 29943-29954.
 21. K. Xiong, X. Jia, Y. Kong, J. Yang, J. Guo, S. Li, M. Adeli, Y. Wang, X. Luo, X. Han and C. Cheng, Customized Covalent Organic Frameworks with in-Plane and Intramolecular Asymmetric Polarization for Superior Hydrogen Peroxide Photosynthesis and Aerobic Oxidation of Alcohol, *Adv. Funct. Mater.*, 2025, **35**, 2510257.
 22. X. Yang, Z.-X. Pan, J.-Y. Yue, X. Li, G. Liu, Q. Xu and G. Zeng, Nitrogen-Site Engineering in Covalent Organic Frameworks for H₂O₂ Photogeneration via Dual Channels of Indirect Two-Electron O₂ Reduction, *Small*, 2024, **20**, 2405907.
 23. M. Liu, S. Yang, X. Yang, C.-X. Cui, G. Liu, X. Li, J. He, G. Z. Chen, Q. Xu and G. Zeng, Post-synthetic modification of covalent organic frameworks for CO₂ electroreduction, *Nat. Commun.*, 2023, **14**, 3800.
 24. L. Zhou, X. Li, K. Cao, Z. Jia, H. Long, Y. Li, G. Tao, N. Liu, J. Zhang and L. Ma, Covalent Organic Framework Membrane with Turing Structures for Deacidification of Highly Acidic Solutions, *Adv. Funct. Mater.*, 2022, **32**, 2108178.
 25. N. A. Khan, R. Zhang, X. Wang, L. Cao, C. S. Azad, C. Fan, J. Yuan, M. Long, H. Wu, M. A. Olson and Z. Jiang, Assembling covalent organic framework membranes via phase switching for ultrafast molecular transport, *Nat. Commun.*, 2022, **13**, 3169.
 26. L. Q. Dong, J. Z. Zhou, L. L. Wu, P. Dong and Z. H. Lin, SERS studies of self-assembled DNA monolayer – characterization of adsorption orientation of oligonucleotide probes and their hybridized helices on gold substrate, *Chem. Phys. Lett.*, 2002, **354**, 458-465.
 27. Y. Hou, X. Pei, Y. Wang, L. Zhang, X. Wei, H. Mao, W. Zhao, S. Zhang and W. Zhang, Selective Detection of Nucleotides in Infant Formula Using an N-Rich Covalent Triazine Porous Polymer, *Journal*, 2022, **12**.
 28. Y. Zhang, Y. Wu, H. Ma, Y. Gao, X. Fan, Y. Zhao, F. Kang, Z. Li, Y. Liu and Q. Zhang, Modulating N-Heterocyclic Microenvironment in β -Ketoenamine Covalent Organic Frameworks to Boost Overall Photosynthesis of H₂O₂, *Small*, 2025, **21**, 2500674.
 29. Y. Zhang, P. He, M. Zhang, J. Zhang, N. He, Y. Zou, Z. Fan, C. Deng, Y. Li and L. Ma, Mild and Subtle Synthesis of β -Ketoenamine COFs with High Crystallinity and Controllable Solubility Guided by a Monomer Preassembly Strategy, *Small*, 2024, **20**, 2407874.
 30. X.-M. Yuan, D.-M.-F. Xiao, C.-L. Zhao and C.-L. Zhang, Enhancing Photocatalytic CO₂RR by Modulating the Active Sites of COF-Based Catalysts, *Small*, 2025, **21**, 2411316.
 31. Z. Zhang, Y. Hou, S. Zhu, L. Yang, Y. Wang, H. Yue, H. Xia, G. Wu, S.-w. Yang and X. Liu, Benzotriazine-Based Covalent Organic Frameworks for Artificial Photosynthesis of H₂O₂ from H₂O, O₂, and Sunlight, *Angew. Chem. Int. Ed.*, 2025, **64**, e202505286.
 32. X. Lan, J. Wang, L. Chen, H. Xu, T. Zhang and Y. Chen, Spatially programmed regioisomeric conjugated microporous polymers modulating zinc sites for selective CO₂ photoreduction to CH₄, *Chem. Sci.*, 2025, **16**, 13893-13904.
 33. T. Lu, A comprehensive electron wavefunction analysis toolbox for chemists, Multiwfn, *The Journal of Chemical Physics*, 2024, **161**, 082503.
 34. W. Weng and J. Guo, The effect of enantioselective chiral covalent organic frameworks and cysteine sacrificial donors on photocatalytic hydrogen evolution, *Nat. Commun.*, 2022, **13**, 5768.
 35. H. Ling, H. Sun, L. Lu, J. Zhang, L. Liao, J. Wang, X. Zhang, Y. Lan, R. Li, W. Lu, L. Cai, X. Bai and W. Wang, Sustainable photocatalytic hydrogen peroxide production over octonary high-entropy oxide, *Nat. Commun.*, 2024, **15**, 9505.
 36. Y. Guo, X. Tong and N. Yang, Photocatalytic and Electrocatalytic Generation of Hydrogen Peroxide: Principles, Catalyst Design and Performance, *Nano Micro Lett.*, 2023, **15**, 77.
 37. L. Fan, X. Bai, C. Xia, X. Zhang, X. Zhao, Y. Xia, Z.-Y. Wu, Y. Lu, Y. Liu and H. Wang, CO₂/carbonate-mediated electrochemical water oxidation to hydrogen peroxide, *Nat. Commun.*, 2022, **13**, 2668.
 38. C. Qin, X. Wu, L. Tang, X. Chen, M. Li, Y. Mou, B. Su, S. Wang, C. Feng, J. Liu, X. Yuan, Y. Zhao and H. Wang, Dual donor-acceptor covalent organic frameworks for hydrogen peroxide photosynthesis, *Nat. Commun.*, 2023, **14**, 5238.
 39. Y. Shao, H. J. M. de Groot and F. Buda, Proton Acceptor near the Active Site Lowers Dramatically the O–O Bond Formation Energy Barrier in Photocatalytic Water Splitting, *The Journal of Physical Chemistry Letters*, 2019, **10**, 7690-7697.
 40. S. M. Carvalho, A. A. P. Mansur, I. B. da Silveira, T. F. S. Pires, H. F. V. Victória, K. Krambrock, M. F. Leite and H. S. Mansur, Nanozymes with Peroxidase-like Activity for Ferroptosis-Driven Biocatalytic Nanotherapeutics of Glioblastoma Cancer: 2D and 3D Spheroids Models, *Journal*, 2023, **15**.
 41. Q. Zhu, L. Shi, Z. Li, G. Li and X. Xu, Protonation of an Imine-linked Covalent Organic Framework for Efficient H₂O₂ Photosynthesis under Visible Light up to 700 nm, *Angew. Chem. Int. Ed.*, 2024, **63**, e202408041.
 42. Z. Xue, B. Zhang, Q. Guo, Y. Wang, Q. Li, K. Yang and S. Qiao, Sacrificial-Agent-Triggered Mass Transfer Gating in Covalent Organic Framework for Hydrogen Peroxide Photocatalysis, *Adv. Mater.*, 2025, **37**, e10201.
 43. C. Zhao, X. Wang, Y. Yin, W. Tian, G. Zeng, H. Li, S. Ye, L. Wu and J. Liu, Molecular Level Modulation of Anthraquinone-containing Resorcinol-formaldehyde Resin Photocatalysts for H₂O₂ Production with Exceeding 1.2 % Efficiency, *Angew. Chem. Int. Ed.*, 2023, **62**, e202218318.



The data that support the findings of this study are available from the corresponding

author upon reasonable request.

